Journal of Materials Science & Technology 217 (2025) 237–244

Contents lists available at ScienceDirect

Journal of Materials Science & Technology

journal homepage: www.elsevier.com/locate/jmst

Research Article

NiTi alloy helical lattice structure with high reusable energy absorption and enhanced damage tolerance

Meng Zhou[a], Haohang Li[a], Zhiwei Xiong[b], Xiang Li[a], Xuyang Li[c], Ying Yang[d], Jie Chen[e], Shijie Hao[a,*]

[a] College of New Energy and Materials, China University of Petroleum, Beijing 102249, China
[b] China Academy of Space Technology, No.104, Youyi Road, Haidian District, Beijing 100094, China
[c] Institute of Advanced Structure Technology, Beijing Institute of Technology, Beijing 100081, China
[d] College of Chemical Engineering and Environment, China University of Petroleum, Beijing 102249, China
[e] Institute of Machinery Manufacturing Technology, China Academy of Engineering Physics, Mianyang 621900, China

ARTICLE INFO

Article history:
Received 5 June 2024
Revised 7 August 2024
Accepted 19 August 2024
Available online 7 September 2024

Keywords:
Helical lattice structure
NiTi shape memory alloy
Reusable energy absorption
Damage tolerance
Additive manufacturing

ABSTRACT

NiTi alloy lattice structures are crucial for reusable energy absorption due to their shape memory effects. However, existing NiTi alloy lattice structures always suffer from localized deformation bands during loading, causing local strains to exceed the recoverable strain limit of the alloy and significantly reducing their reusable energy-absorbing capacity. In this study, we developed a NiTi alloy helical lattice structure (HLS) to effectively prevent localized deformation bands. This is attributed to its struts distributing stress and strain uniformly through torsional deformation, thereby alleviating local stress concentrations and suppressing the formation of localized deformation bands. Additionally, its unit cells provide mutual support and reinforcement during deformation, effectively preventing the progression of localized deformation bands. The NiTi alloy HLS exhibits superior reusable energy absorption compared to previously reported reusable energy-absorbing materials/structures and enhanced damage tolerance under large compression strain. This study provides valuable insights for the development of high-performance reusable NiTi alloy energy-absorbing lattice structures.

1. Introduction

Reusable energy-absorbing lattice structures are urgently needed in various fields, such as repetitive buffered landings of spacecraft [1] and repeated energy absorption for protective equipment [2]. These structures must regain their original shape after absorbing energy through deformation. Conventional energy-absorbing lattice structures, such as aluminum honeycombs [3] and 316 L stainless steel lattice structures [4], fail to meet these requirements because they absorb energy through severe plastic deformation and fracture, which are irreversible. Nickel-titanium (NiTi) shape memory alloys exhibit the shape memory effect [5] that enables them to recover their original shape through heating after deformation, thereby possessing the potential to fabricate reusable energy-absorbing lattice structures. The shape memory effect of NiTi alloy arises from the reversible martensitic phase transformation, theoretically capable of generating up to 6 % recoverable strain [6]. Therefore, when NiTi alloy energy-absorbing lattice structures undergo deformations of up to tens of percent to absorb energy, the localized strains must not exceed 6 % to ensure they can recover their original shape during subsequent heating processes.

However, existing NiTi alloy energy-absorbing lattice structures, such as NiTi gradient lattice structures [7] and NiTi bionic lattice structures [8], exhibit noticeable localized deformation bands under tens of percent strain. In the region of localized deformation bands, localized strain exceeds the recoverable strain limit of NiTi alloy (6 %), leading to irreversible plastic deformation and fracture damage. This significantly reduces the reusable energy-absorbing capacity of these structures. The formation of localized deformation bands is primarily caused by intense local stress concentrations during the structural deformation process [9,10]. Thus, NiTi alloy energy-absorbing lattice structures must be specifically designed to alleviate local stress concentrations and prevent localized deformation bands to ensure superior reusable energy-absorbing capacity.

Helical structures are prevalent in both natural and engineering fields, such as the helical tendrils [11] of climbing plants and coil

* Corresponding author.
E-mail address: haoshijie@cup.edu.cn (S. Hao).

https://doi.org/10.1016/j.jmst.2024.08.032
1005-0302/

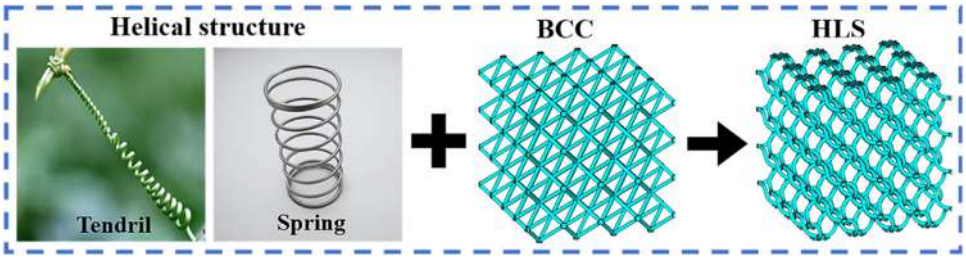

Fig. 1. Schematic of the design concept for the HLS.

springs [12] in mechanical engineering. Their continuous geometries [13] can effectively alleviate stress and strain concentrations in localized areas caused by abrupt shape changes [14] during deformation. More importantly, when subjected to force, they can transfer stress along the helical direction through torsional deformation to achieve uniform stress and strain distribution [15]. Consequently, helical structures can alleviate stress concentrations and avoid the formation of localized deformation bands throughout the deformation process [16]. This makes them suitable for designing NiTi alloy energy-absorbing structures. However, an individual helical structure typically has low specific strength [17,18] and specific energy absorption. To improve its energy-absorbing capacity, it should be integrated with high-specific energy-absorption lattice structures, such as body-centered cubic (BCC) lattice structures [19].

In this study, we combined the helical structure with the BCC lattice structure to create a novel helical lattice structure (HLS), as illustrated in Fig. 1. Under large compressive strains ($\geq$ 40 %), the HLS lattice structure exhibits an absence of localized deformation bands and demonstrates superior reusable energy absorption. Furthermore, the HLS lattice structure shows enhanced damage tolerance compared to the BCC lattice structure. This study offers significant insights into the development of high-performance reusable NiTi alloy energy-absorbing lattice structures.

2. Experimental procedure

The HLS lattice structure was modeled using SOLIDWORKS software. The unit cell of the HLS lattice structure was initially established, as shown in Fig. 2(a). This unit cell includes three geometric parameters: the unit cell size L = 8 mm, the strut diameter D = 0.8 mm, and the helical diameter of the strut D_h = 1.8 mm. The unit cell was then arrayed along the *x*, *y*, and *z* directions to form the HLS lattice structure, with the number of arrays being 4. To ensure consistency in subsequent comparisons, the parameters *L*, *D*, and the array number of the conventional BCC lattice structure were kept the same as those of the HLS lattice structure. All these lattice structures were fabricated using an Eplus M100-T SLM machine equipped with a 200 W ytterbium-fiber laser. The nominal composition of the NiTi powder is $Ni_{50.5}Ti_{49.5}$ (at%), and the particle size distribution ranges from 15 to 53 μm. The SLM process parameters during sample preparation are identical to those used in the study [20]. The final NiTi alloy lattice structures are shown in Fig. 2(b).

Uniaxial compression experiments on NiTi lattice structures were conducted at room temperature (RT) using a KQL universal testing machine, as illustrated in Fig. 2(c). The compression direction was along the building direction (z-axis), and the loading and unloading rates were set at 1×10^{-3} s^{-1}. After compression, the deformed structures were immersed in hot water (~100 °C) for 1 min to recover their original shape. The shape-recovered structures were then cooled to room temperature before undergoing the next round of compression and recovery experiments. The compression deformation and shape recovery processes were recorded by a camera. Stress was calculated by dividing the load by the original cross-sectional area perpendicular to the direction of the structure. The strain was calculated by dividing the displacement of the upper indenter by the initial height of the structure. The shape recovery rate (R_{rec}) for each cycle was determined by

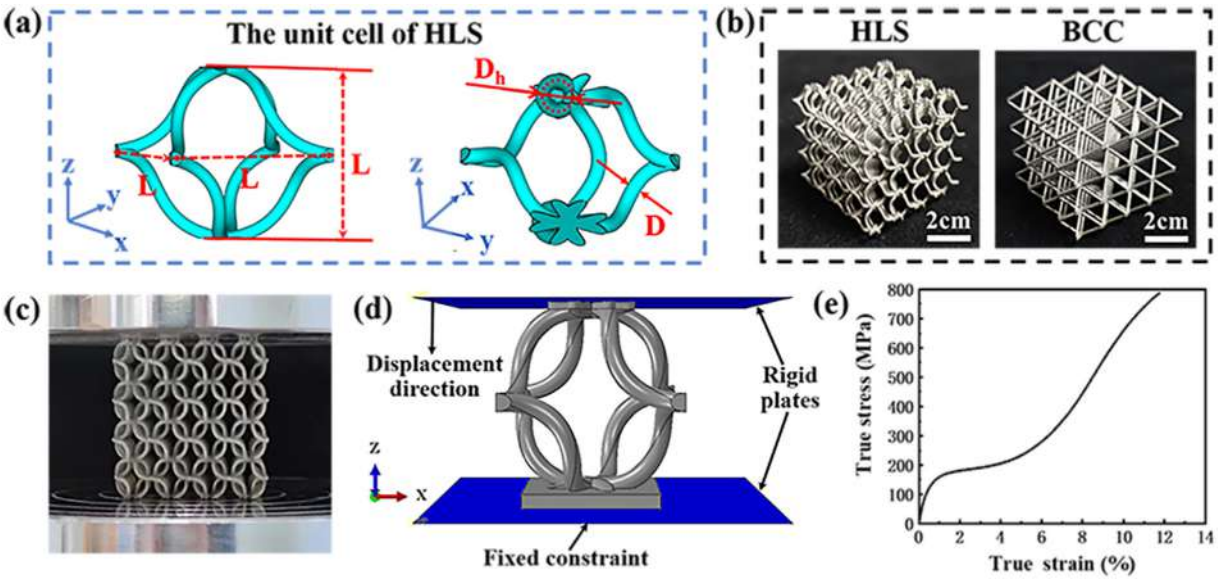

Fig. 2. (a) Model of the unit cell for the HLS lattice structure. (b) Photographs of the HLS and BCC lattice structures. (c) Photograph of the compression process. (d) FEA model. (e) True stress-strain curve of the NiTi alloy fabricated by SLM under uniaxial tension.

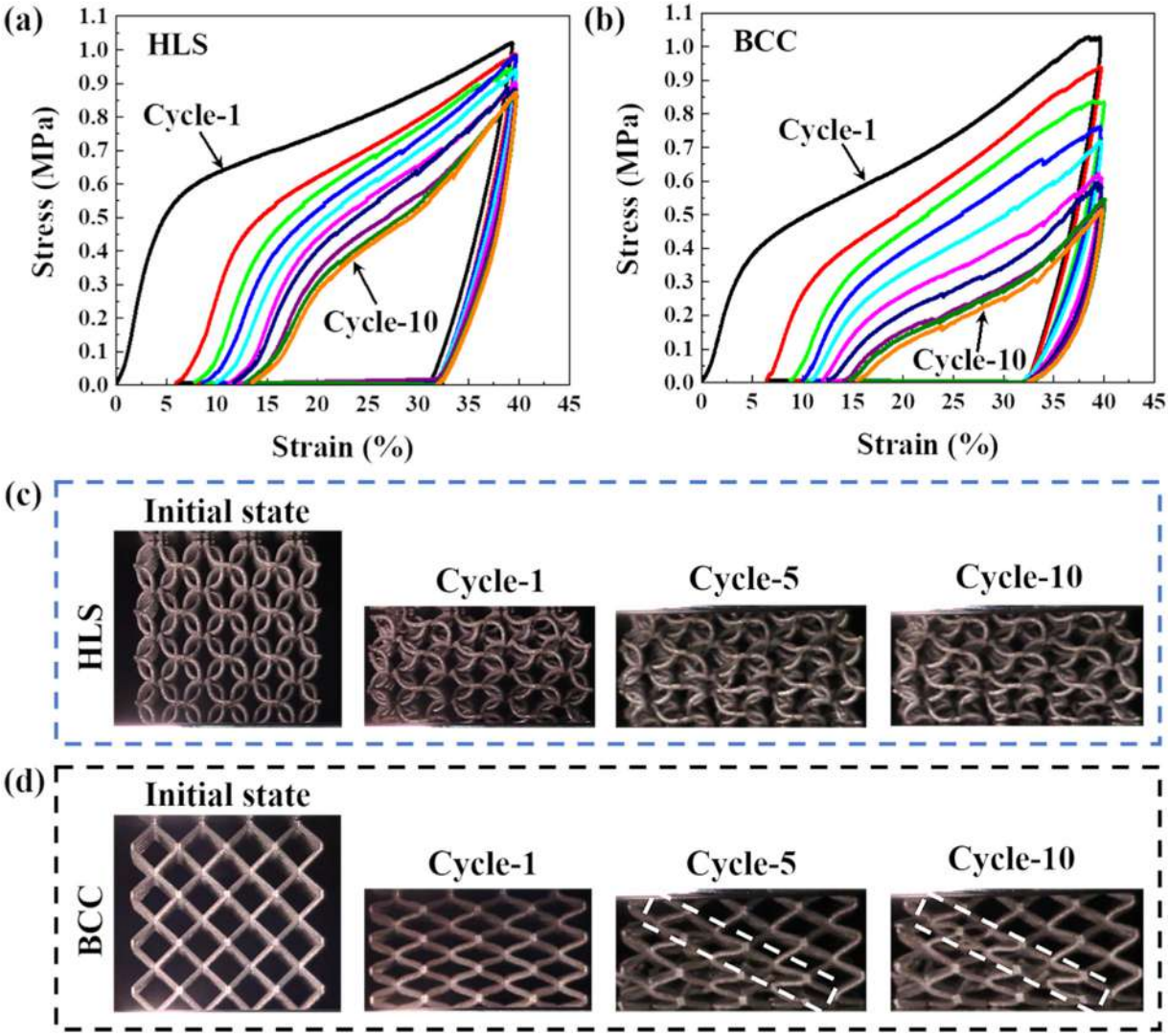

Fig. 3. (a, b) Cyclic compressive stress-strain curves of (a) HLS and (b) BCC. (c, d) Deformation behavior photographs of (c) HLS and (d) BCC.

the ratio of the height after heat recovery to the original height. The specific energy absorption (SEA) per unit volume was obtained by integrating the stress-strain curve. The maximum stress on the stress-strain curve was denoted by σ_{max}.

Finite element analysis (FEA) was conducted using ABAQUS software to investigate the deformation behavior and strain distribution of lattice structures, utilizing static general analysis methods. The FEA model, depicted in Fig. 2(d), primarily comprises a unit cell of lattice structure and rigid plates at both ends. The bottom rigid plate was fully fixed, and the top rigid plate was subjected to only downward displacement. The mesh type for the unit cell of the lattice structure was C3D8R. The rigid plates were specified as analytical rigid bodies, and the contact type between them was defined as surface-to-surface contact. The material parameters of the NiTi alloy were defined by the uniaxial tensile true stress-strain curve shown in Fig. 2(e).

3. Results and discussion

Fig. 3(a, b) displays the cyclic compressive stress-strain responses of the HLS and BCC lattice structures, respectively. A comparative analysis of the residual strain and compressive stress decay during each cycle indicates that the HLS lattice structure demonstrates superior cyclic stability compared to the BCC lattice structure. Fig. 3(c, d) depicts the snapshots of the initial state and 40 % strain compression of these lattice structures. As the number of cycles increases, no significant localized deformation bands are observed in the HLS lattice structure. In contrast, a localized deformation band, marked by white dashed boxes in Fig. 3(d), emerges in the BCC lattice structure. In this localized deformation band, the struts of the BCC lattice structure experience fracture and damage, resulting in diminished mechanical performance during the cycling process. Conversely, the HLS lattice structure effectively suppresses the formation of localized deformation bands and exhibits superior mechanical performance during the cyclic process.

Fig. 4 provides a detailed analysis of the shape recovery, energy absorption, and load-carrying characteristics of the HLS and BCC lattice structures during the cyclic process. Fig. 4(a, b) presents snapshots illustrating the shape recovery process of these two structures. Fig. 4(c) shows the R_{rec} after each cycle, indicating that the R_{rec} of the HLS lattice structure consistently exceeds that of the BCC lattice structure. This higher R_{rec} in the HLS lattice structure is attributed to the suppression of localized deformation bands, resulting in less irrecoverable plastic deformation and damage. Fig. 4(d, e) depicts the variation of SEA and σ_{max} with the number of cycles for both structures, respectively. The SEA of both structures decreases as the number of cycles increases, yet the SEA of

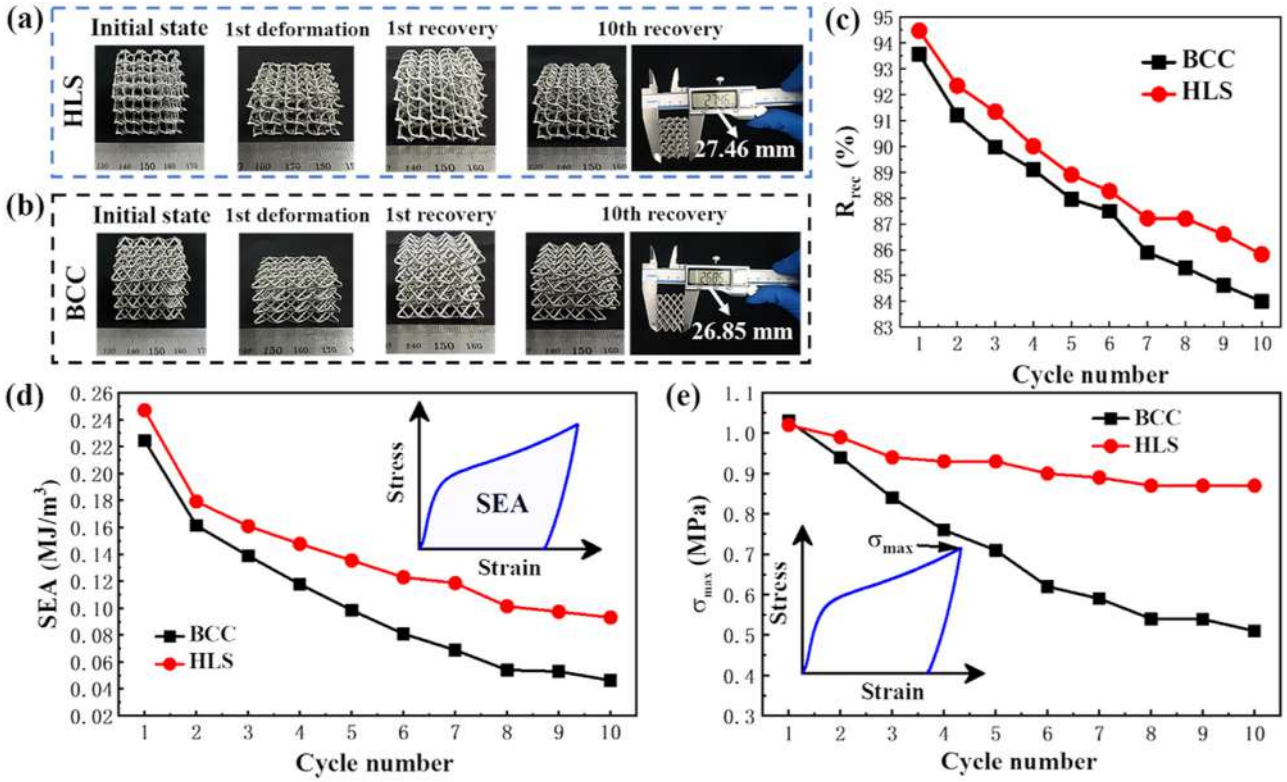

Fig. 4. (a, b) Shape recovery process of (a) HLS and (b) BCC. (c) Evolution of R_{rec} during the cycling process of HLS and BCC. (d, e) Evolution of (d) SEA and (e) σ_{max} during the cycling process of HLS and BCC. The inset depicts the definition of SEA and σ_{max}.

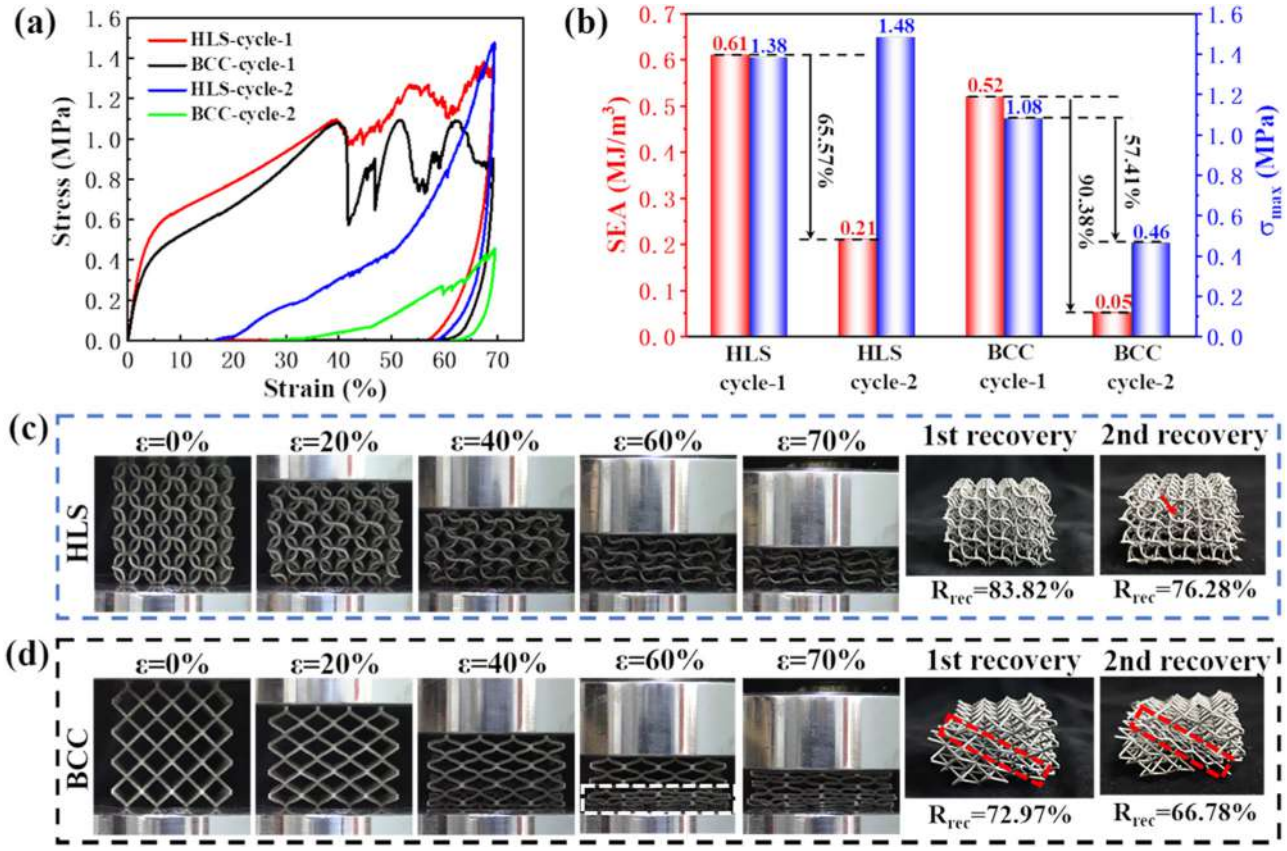

Fig. 5. (a) Cyclic compressive stress-strain curves under overload conditions for HLS and BCC. (b) Evolution of SEA and σ_{max} during the cycling process for HLS and BCC. (c, d) Photographs of the deformation and shape recovery process of (c) HLS and (d) BCC. The inconsistency in the localized deformation bands marked with white and red dashed boxes is caused by the different camera shooting directions.

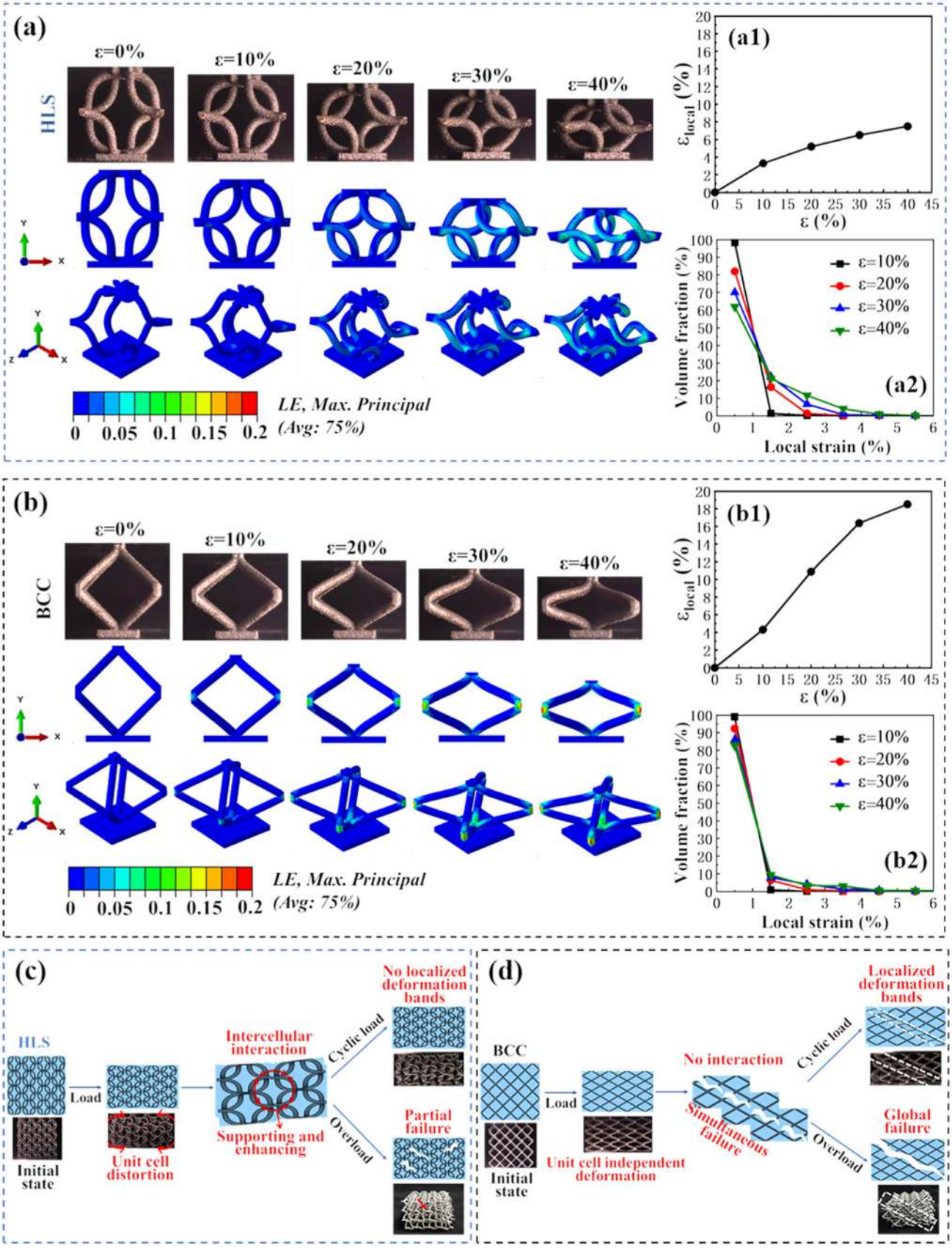

Fig. 6. (a, b) Deformation behavior and FEA results of the (a) HLS and (b) BCC lattice structure unit cells. (c, d) Schematic diagram of the deformation behavior of (c) HLS and (d) BCC lattice structures.

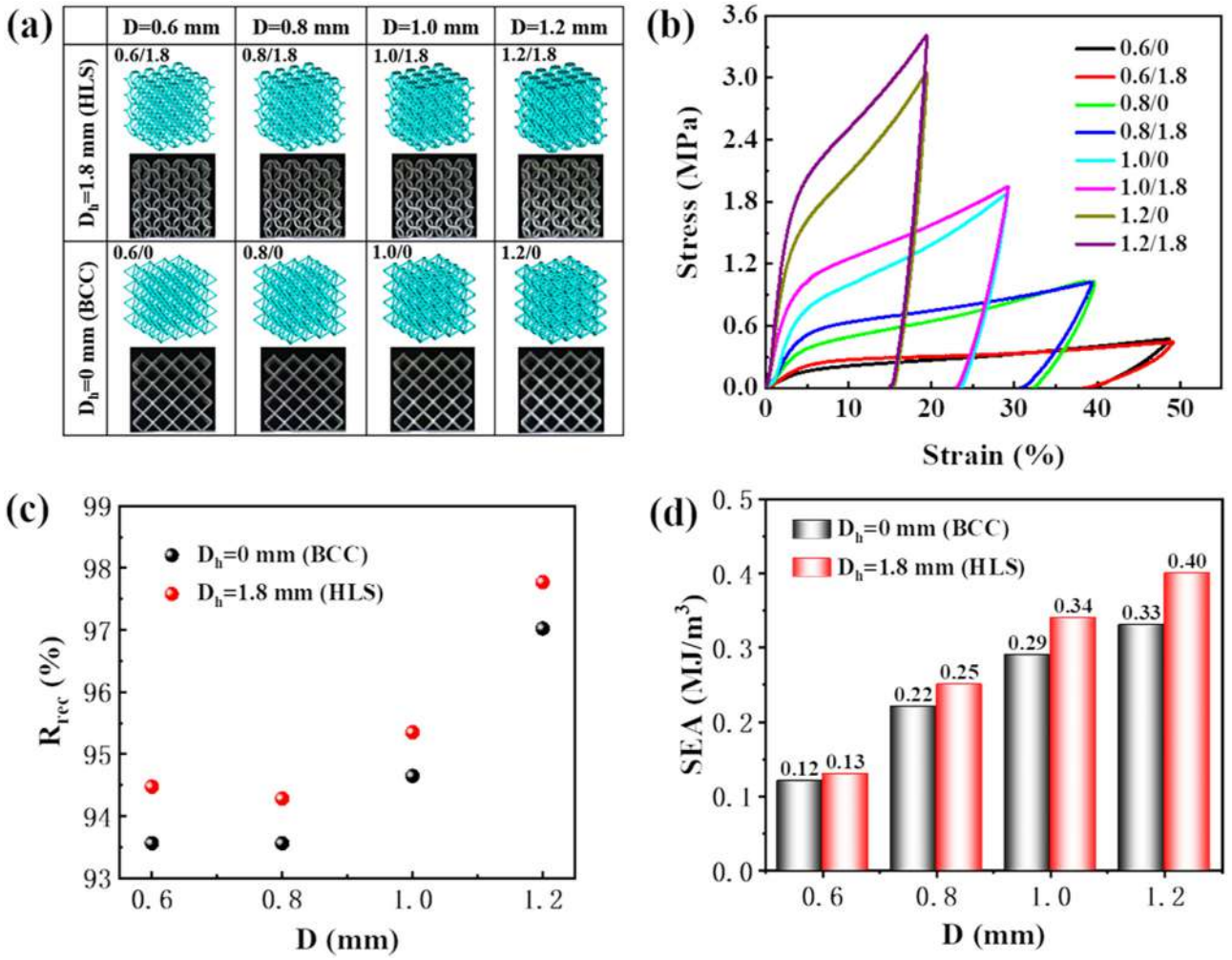

Fig. 7. (a) Models and sample photographs of HLS and BCC structures with different strut diameters. (b) Stress-strain curve of HLS and BCC structures with different strut diameters. (c) R_{rec} and (d) SEA of HLS and BCC structures with different strut diameters.

the HLS lattice structure consistently remains higher than that of the BCC lattice structure. This indicates that the HLS lattice structure has superior cyclic energy-absorbing capacity. Due to the suppression of localized deformation bands, the σ_{max} of the HLS lattice structure is only slightly reduced during the cycling process. In contrast, the σ_{max} of the BCC lattice structure undergoes a substantial decrease. This indicates that the HLS lattice structure has better cyclic load-carrying capacity.

Secondly, to investigate the damage tolerance of HLS and BCC lattice structures under overloaded conditions, both were subjected to two compression deformation cycles at 70 % strain. The resulting stress-strain curves are shown in Fig. 5(a). During the first compression, both structures exhibited stress fluctuations as the strain gradually increased, indicating that they experienced varying degrees of damage. The HLS lattice structure exhibits smoother stress fluctuations compared to the BCC lattice structure. During the second compression, the HLS lattice structure demonstrates higher strength compared to the BCC lattice structure. The SEA and σ_{max} for the two compression processes are illustrated in Fig. 5(b). Compared to the first compression, the SEA of the HLS lattice structure decreased by 65.57 % during the second compression, while the BCC lattice structure experienced a 90.38 % decrease. The σ_{max} of the HLS lattice structure remained nearly constant, whereas that of the BCC lattice structure decreased by 57.41 %. These findings suggest that, compared to the BCC lattice structure, the HLS lattice structure exhibits enhanced energy absorption and load-bearing capacity after experiencing damage.

Fig. 5(c, d) depicts snapshots of these two structures during the first compression and subsequent heating recovery. The complete record of the initial heating recovery process is available in Supplementary Data Video S1. The HLS lattice structure exhibited no significant localized deformation bands throughout the entire compression process and demonstrated progressive failure, corresponding to smoother stress fluctuations. In contrast, the BCC lattice structure displayed evident localized deformation bands during compression, as illustrated by the white dashed box in Fig. 5(d). This led to a sudden decrease in mechanical properties and severe stress fluctuations. After heat recovery, the HLS structure remained intact with only some struts damaged, as indicated by the red arrows in Fig. 5(c). In contrast, the BCC lattice structure experienced global failure, as shown by the red dashed box in Fig. 5(d). The R_{rec} of the HLS structure is higher than that of the BCC structure during both heating recovery processes. These findings indicate that the HLS lattice structure possesses superior damage-tolerant capability under overload conditions.

Subsequently, we conducted finite element analysis (FEA) on the deformation behaviors of HLS and BCC lattice structures to elucidate the mechanism by which the HLS structure suppresses localized deformation bands. Fig. 6(a, b) shows snapshots of HLS and BCC lattice structure unit cells during compression, along with

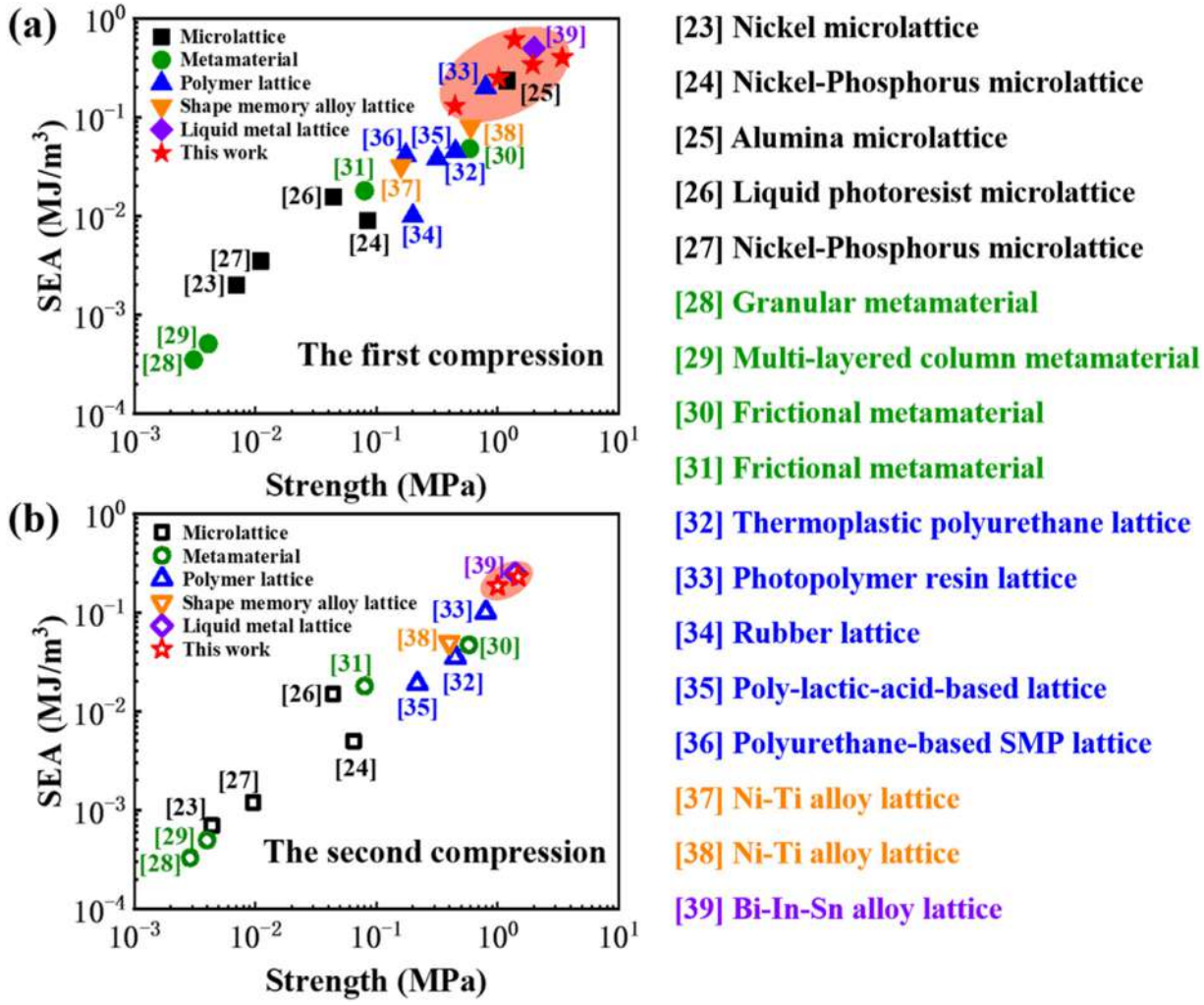

Fig. 8. (a) Ashby maps of strength and SEA under the first compression. (b) Ashby maps of strength and SEA under the second compression. Due to the absence of secondary compression data in some references, the data points in (b) are relatively sparse.

their corresponding FEA results. The simulated force-strain curves of their unit cells are shown in Fig. S1 in Supplementary materials, and the FEA results align well with the experimental data. The results reveal that the struts of the HLS lattice structure exhibit twisting deformation during loading, leading to relatively low and uniformly distributed local strains. In contrast, the struts of the BCC lattice structure exhibit bending deformation, resulting in significant stress concentration near the nodes and high local strains. Statistical analysis of the maximum local strain (ε_{local}) under identical compressive strain conditions, as shown in Fig. 6(a1, b1), indicates that the ε_{local} of the HLS lattice structure is consistently lower than that of the BCC lattice structure. At 40 % compressive strain, the ε_{local} of the HLS lattice structure is 7.5 %, whereas the ε_{local} of the BCC lattice structure reaches 18.5 %, due to stress concentration at its nodes. This exceeds the recoverable strain limit (6 %) of NiTi alloy, resulting in poor cyclic energy-absorbing capacity for BCC lattice structures. Fig. 6(a2, b2) depicts the volume fraction of the elements within the specified range of local strain for both structures, as determined by the FEA results. With increasing compressive strain, the volume distribution curve of the HLS lattice structure gradually flattens, indicating a more uniform strain distribution and reduced stress concentration. In contrast, the volume fraction of the BCC lattice structure remains almost unchanged, reflecting ineffective stress concentration mitigation. These findings demonstrate that the struts of the HLS lattice structure achieve uniform stress distribution and transmission through twisting deformation, effectively alleviating stress concentration and suppressing localized deformation bands.

Moreover, the mutual support among unit cells in the HLS lattice structure further suppresses the progression of localized deformation bands, preventing global fracture during the deformation process. As illustrated in the simplified schematic in Fig. 6(c), the unit cells in the HLS lattice structure twist under the loading process, resulting in significant intercellular interactions. These interactions enable the unit cells to mutually support and reinforce each other during deformation, effectively suppressing the progression of localized deformation bands under cyclic compression [21]. Under overloaded conditions, this interaction also impedes the continuous progression of failure, leading to only partial failure of the structure and demonstrating favorable damage tolerance. In contrast, the unit cells in the BCC lattice structure deform independently, lacking intercellular interactions, as shown in Fig. 6(d). This independence leads to the simultaneous failure of unit cells during deformation [22], culminating in the formation of localized deformation bands and global failure. Therefore, the HLS lattice structure effectively inhibits the formation and progression of localized deformation bands, demonstrating excellent energy-absorbing capacity and enhanced damage tolerance.

We further investigated the energy absorption and recovery properties of HLS and BCC lattice structures with varying strut

diameters to validate the applicability of the helical design strategy. The models and photographs of HLS and BCC lattice structures with four different strut diameters are presented in Fig. 7(a). The strut diameters (D) are 0.6, 0.8, 1.0, and 1.2 mm, respectively, and the helical diameter (D_h) remains constant at 1.8 mm for the HLS lattice structures and 0 mm for the BCC lattice structures. These lattice structures are denoted as D/D_h, for example, 0.6/1.8 means $D = 0.6$ mm and $D_h = 1.8$ mm. Fig. 7(b) provides the compressive stress-strain curves for these structures. The strength of these structures increases with increasing strut diameter, while the strain decreases. The R_{rec} values at different strut diameters are illustrated in Fig. 7(c). It can be seen that the R_{rec} of the HLS lattice structures is consistently higher than that of the BCC lattice structures. Fig. 7(d) compares the SEA for these structures. The HLS lattice structures consistently exhibit higher SEA than the BCC lattice structures across various strut diameters. This indicates that the helical design strategy is universally applicable to lattice structures with varying strut diameters within a certain range.

Finally, we compared the strength and SEA of a series of HLS lattice structures in this work with those of previously reported reusable energy-absorbing materials/structures [23-39], as shown in Fig. 8. The detailed material and structural features of these reusable energy-absorbing materials/structures are provided in Table S1. Specifically, Fig. 8(a) presents the Ashby maps of strength versus SEA for these materials/structures under the first compression. The HLS lattice structures developed in this work exhibit superior strength and SEA compared to almost all previously reported reusable energy-absorbing materials/structures. Furthermore, the HLS lattice structures demonstrate outstanding cyclic energy absorption capabilities. During the second compression, their strength and SEA remain superior to those of almost all reported materials/structures, as shown in Fig. 8(b).

4. Conclusions

In summary, the NiTi alloy HLS lattice structure developed in this study effectively suppresses the formation of local deformation bands through the twisting deformation of struts and the mutual support and enhancement between unit cells. It demonstrates enhanced damage tolerance under high compression strain and superior reusable energy absorption compared to previously reported reusable energy-absorbing materials/structures. This helical design strategy can be applied to lattice structures with varying strut diameters to meet diverse application requirements. This study contributes to promoting the development of high-performance reusable NiTi alloy energy-absorbing lattice structures.

Declaration of competing interest

The authors declare that they have no known competing financial interests or personal relationships that could have appeared to influence the work reported in this paper.

CRediT authorship contribution statement

Meng Zhou: Writing – original draft, Methodology, Formal analysis, Data curation, Conceptualization. **Haohang Li:** Methodology, Formal analysis, Conceptualization. **Zhiwei Xiong:** Methodology, Data curation, Conceptualization. **Xiang Li:** Methodology, Formal analysis. **Xuyang Li:** Methodology, Data curation. **Ying Yang:** Writing – review & editing. **Jie Chen:** Methodology, Data curation. **Shijie Hao:** Writing – review & editing, Methodology, Funding acquisition, Formal analysis, Conceptualization.

Acknowledgments

This work was financially supported by the National Key R&D Program of China (No. 2022YFB4600500) and the National Safety Academic Fund (Nos. U2130201 and U2330105).

Supplementary materials

Supplementary material associated with this article can be found, in the online version, at doi:10.1016/j.jmst.2024.08.032.

References

[1] W. Dongliang, C. Qifeng, L.M. Luohaijun, in: Proceedings of the 8th Eur. Conf. Aeronaut. Aerosp. Sci. Eucass Madr., Spain, 2019, pp. 1–4.
[2] S. Chen, X. Tan, J. Hu, S. Zhu, B. Wang, L. Wang, Y. Jin, L. Wu, Compos. Part B-Eng. 215 (2021) 108745.
[3] Y. Zhang, Q. Liu, Z. He, Z. Zong, J. Fang, Compos. Part B-Eng. 156 (2019) 17–27.
[4] T. Zhong, K. He, H. Li, L. Yang, Mater. Des. 181 (2019) 108076.
[5] S.Kumar Patel, B. Swain, R. Roshan, N.K. Sahu, A. Behera, Mater. Today Proc. 33 (2020) 5552–5556.
[6] K. Otsuka, X. Ren, Prog. Mater. Sci. 50 (2005) 511–678.
[7] W. Chen, D. Gu, J. Yang, Q. Yang, J. Chen, X. Shen, Int. J. Extreme Manuf. 4 (2022) 045002.
[8] J. Sun, D. Gu, K. Lin, L. Yuan, J. Yang, W. Chen, Smart Mater. Struct. 31 (2022) 074003.
[9] X. Liu, T. Wada, A. Suzuki, N. Takata, M. Kobashi, M. Kato, Mater. Des. 199 (2021) 109416.
[10] L. Bai, Y. Xu, X. Chen, L. Xin, J. Zhang, K. Li, Y. Sun, Mater. Des. 211 (2021) 110140.
[11] S.J. Gerbode, J.R. Puzey, A.G. McCormick, L. Mahadevan, Science 337 (2012) 1087–1091.
[12] D. Pastorcic, G. Vukelic, Z. Bozic, Eng. Fail. Anal. 99 (2019) 310–318.
[13] S. Wang, S. Lei, J. Zhou, H. Xiao, J. Mech. Sci. Technol. 24 (2010) 1203–1210.
[14] Z. Li, Y. Nie, B. Liu, Z. Kuai, M. Zhao, F. Liu, Mater. Des. 192 (2020) 108709.
[15] M.A. Savi, P.M.C.L. Pacheco, M.S. Garcia, R.A.A. Aguiar, L.F.G. De Souza, R.B. Da Hora, Smart Mater. Struct. 24 (2015) 035012.
[16] H. Tripolt, C.J. Burstone, P. Bantleon, W. Manschiebel, Am. J. Orthod. Dentofac. Orthop. 115 (1999) 498–507.
[17] J. Wu, M. Sang, J. Zhang, Y. Sun, X. Wang, J. Zhang, H. Pang, T. Luo, S. Pan, S. Xuan, X. Gong, Small 19 (2023) 2207454.
[18] Y. Gao, F. Guo, P. Cao, J. Liu, D. Li, J. Wu, N. Wang, Y. Su, Y. Zhao, ACS Nano 14 (2020) 3442–3450.
[19] M. Liu, N. Takata, A. Suzuki, M. Kobashi, J. Mater. Sci. Technol. 36 (2020) 106–117.
[20] Z. Xiong, Z. Li, Z. Sun, S. Hao, Y. Yang, M. Li, C. Song, P. Qiu, L. Cui, J. Mater. Sci. Technol. 35 (2019) 2238–2242.
[21] X. Wang, X. Li, Z. Li, Z. Wang, W. Zhai, Small 20 (2024) 2307369.
[22] C. Liu, J. Lertthanasarn, M.-S. Pham, Nat. Commun. 12 (2021) 4600.
[23] L. Salari-Sharif, T.A. Schaedler, L. Valdevit, J. Mater. Res. 29 (2014) 1755–1770.
[24] X. Zheng, W. Smith, J. Jackson, B. Moran, H. Cui, D. Chen, J. Ye, N. Fang, N. Rodriguez, T. Weisgraber, C.M. Spadaccini, Nat. Mater. 15 (2016) 1100–1106.
[25] L.R. Meza, S. Das, J.R. Greer, Science 345 (2014) 1322–1326.
[26] T. Frenzel, C. Findeisen, M. Kadic, P. Gumbsch, M. Wegener, Adv. Mater. 28 (2016) 5865–5870.
[27] T.A. Schaedler, A.J. Jacobsen, A. Torrents, A.E. Sorensen, J. Lian, J.R. Greer, L. Valdevit, W.B. Carter, Science 334 (2011) 962–965.
[28] K. Fu, Z. Zhao, L. Jin, Adv. Funct. Mater. 29 (2019) 1901258.
[29] Y. Chen, L. Jin, Adv. Funct. Mater. 31 (2021) 2102113.
[30] P. Jiang, S. Zhang, H. Yang, Y. Li, ACS Appl. Mater. Interfaces 15 (2023) 43102–43110.
[31] Y. Wang, B. Ramirez, K. Carpenter, C. Naify, D.C. Hofmann, C. Daraio, Extreme Mech. Lett. 33 (2019) 100557.
[32] S. Yuan, F. Shen, J. Bai, C.K. Chua, J. Wei, K. Zhou, Mater. Des. 120 (2017) 317–327.
[33] M. Keshavarzan, M. Kadkhodaei, F. Forooghi, Polym. Test. 91 (2020) 106832.
[34] Z. Wang, R. Bo, H. Bai, S. Cao, S. Wang, J. Chang, Y. Lan, Y. Li, Y. Zhang, ACS Appl. Mater. Interfaces 15 (2023) 22553–22562.
[35] K. Dong, Y. Wang, Z. Wang, W. Qiu, P. Zheng, Y. Xiong, Compos. Part Appl. Sci. Manuf. 169 (2023) 107529.
[36] M. Bodaghi, A. Serjouei, A. Zolfagharian, M. Fotouhi, H. Rahman, D. Durand, Int. J. Mech. Sci. 173 (2020) 105451.
[37] X. Li, H. Wang, L. Sun, X. Wang, Y. Pan, M. Zhou, X. Guo, ACS Appl. Mater. Interfaces 15 (2023) 53746–53754.
[38] Z. Xiong, M. Li, S. Hao, Y. Liu, L. Cui, H. Yang, C. Cui, D. Jiang, Y. Yang, H. Lei, Y. Zhang, Y. Ren, X. Zhang, J. Li, ACS Appl. Mater. Interfaces 13 (2021) 39915–39924.
[39] F. Deng, Q.-K. Nguyen, P. Zhang, Appl. Mater. Today 29 (2022) 101671.